From synthesis to fabrication: Engineering thin translucent films with green persistent luminescent nanoparticles

Douglas L. Fritzen [a], Gabriel Nardy [a], Marcelo C. Portes [a], Luidgi Giordano [a,b], Everton Bonturim [c], Verônica C. Teixeira [d], Lucas C.V. Rodrigues [a,*]

[a] *Department of Fundamental Chemistry, Institute of Chemistry, University of São Paulo, CEP 05508-000, São Paulo, SP, Brazil*
[b] *PSL Research University, Chimie-ParisTech, IRCP, CNRS UMR8247, 11 Rue P&M Curie, 75005, Paris, France*
[c] *Department of Chemistry, School of Engineering, Mackenzie Presbyterian University, 01302-907, São Paulo, SP, Brazil*
[d] *Brazilian Synchrotron Light Laboratory (LNLS), Brazilian Center for Research in Energy and Materials (CNPEM), 13083-970, Campinas, SP, Brazil*

ABSTRACT

Green-emitting $ZnGa_2O_4$:Mn^{2+} persistent luminescent nanoparticles were synthesized via a solvothermal method followed by a microwave-assisted sintering at 1150 °C. The obtained cubic-like particles averaged 62 ± 16 nm by Transmission Electron Microscopy (TEM) and presented afterglow for up to 2 h after a 5 min excitation in the UV. By Electron Paramagnetic Resonance (EPR), it was observed that the Mn^{2+} dopant replaces uniquely Zn^{2+} sites during synthesis. The obtained particles were dispersed with hydroxypropyl methylcellulose (HPMC) in water to create thin films by drop-casting. The films with different concentrations of nanoparticles (1 g/m², 10 g/m² and 100 g/m²) had average visible transmittances between 20% and 24%, and presented persistent luminescence after UV excitation, with longer duration by increasing nanoparticle concentration. By synchrotron X-ray Fluorescence (XRF) nanomapping of these films it is possible to see clusters of up to 6 μm of the nanoparticles in the film due to water pockets during film-casting. The X-ray Excited Optical Luminescence (XEOL) showed only Mn^{2+} emission and the XEOL-XRF mapping proved the integrity of the nanoparticles after film fabrication. By combining the solvothermal method, microwave-assisted sintering, and drop casting, this study establishes a promising pathway for the development of advanced flexible and translucent persistent luminescent composites.

1. Introduction

Persistent luminescent (PersL) materials, for the most part, are found as inorganic solid crystals doped with an activator center (usually d-block and/or f-block metals). Activators are mainly responsible for the phenomenon of photoluminescence in crystals, attributing very well-defined excitation and emission spectra to materials [1–7]. The energy storing occurs in trapping centers within the material and the releasing occurs by thermal energy absorption, resulting in a glow phenomenon that can last from a few seconds to hours after ceasing the irradiation source [8–10]. The traps are impurities, (co-)dopants or lattice defects (natural or doping-induced) in the inorganic matrix, which creates energy levels within the band gap energy of the material. Innumerous PersL materials are currently known, ranging from UV to NIR emitters [11].

Their applicability is intrinsically related to the emission wavelength, as well as the physical and chemical properties of the material. For instance, one of the most well-known PersL materials is the blue-emitter $Sr_2MgSi_2O_7$:Eu^{2+},Dy^{3+} featuring applications on e.g. forensic chemistry, LEDs, fibers, films and glasses [12–14]. On the green-emitters

list, $ZnGa_2O_4$:Mn^{2+} has grown attention, with studies on novel transparent single-crystals PersL materials and thin-films production [12,15, 16]. Furthermore, $ZnGa_2O_4$:Mn^{2+} (ZGO) spinel compounds featuring persistent luminescence are suitable materials for a wide range of application, e.g. vacuum electroluminescent displays (VEDs), field emission displays (FEDs), light emitting diodes (LEDs), solid-state lasers, UV photodetectors, thermally and optically stimulated dosimeters, anticounterfeiting and long persistent materials [17–20]. To increase the range of applications, one strategy is to produce novel materials or composites with specific properties that are not usually found in usual PersL compounds. One trending property for PersL materials is transparency. Transparent materials featuring PersL properties might be applied on bioreactor installations for extended photosynthesis during dark times, as visual indicators of UV or X-ray irradiation, or novel electronic devices, such as in a new generation of AC-LEDs.

Recently, our group reported the production of translucent cellulose-based composites, featuring PersL on blue region and great transmittance on the visible range [12]. The methodology of the film deposition achieved homogeneous dispersion of inorganic particles within the organic matrix. In this context, this work aims to expand the
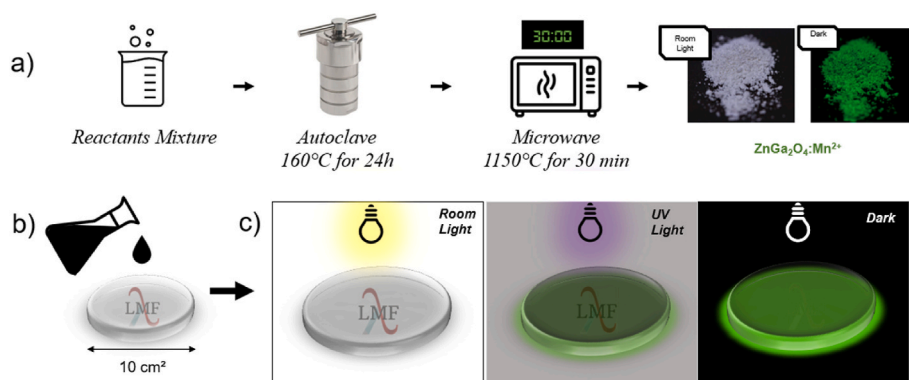

Fig. 1. Schematic representation (a) of the ZGO synthesis procedure and of the (b) film casting procedure. (c) Representation of luminescent and translucent properties of produced HPMC/nZGO:Mn^{2+}.

methodology of translucent PerL composites production to produce a green emitter translucent PersL composite. For that, the synthesis and optimization of Zn Ga$_2$O$_4$:Mn^{2+}-nanoparticles combining hydrothermal synthesis method and microwave annealing, aiming to enhance the optical properties of ZGO:Mn^{2+} nanoparticles (nZGO:Mn^{2+}) is reported. Furthermore, the so obtained nZGO:Mn^{2+} was applied to hydroxypropyl methylcellulose (HPMC) films in order to create a thin-film composite, following the method of drop-casting thin-film deposition and the optical properties of the film are studied regarding its transparency and persistent luminescence.

2. Experimental section

2.1. Materials

ZnO (Sigma Aldrich 99,0%); Ga$_2$O$_3$ (Sigma Aldrich 99,99%); Mn (NO$_3$)$_2$ (Sigma Aldrich >97,0%); HNO$_3$ concentrated (Sigma Aldrich); Toluene (Sigma Aldrich, 99,8%); Oleic acid (Sigma Aldrich technical degree); NaOH (Sigma Aldrich 97,0%) were used as raw materials without further purification.

2.2. nZGO:Mn^{2+} synthesis procedure

The synthesis of the ZnGa$_2$O$_4$:Mn^{2+} (0.05% of Mn^{2+} in mole% of Zn^{2+}) was a modification of the one reported by Srivastava et al. [21] and it was carried out by converting the metal oxides (Ga$_2$O$_3$ and ZnO) into their corresponding nitrates solution with an excess of concentrated HNO$_3$. Then, 2 mmol of Ga(NO$_3$)$_3$, 0.9995 mmol of Zn(NO$_3$)$_2$ and 0.0005 mmol of Mn(NO$_3$)$_2$ were stirred, the pH was adjusted to 10 with

NaOH 1 M and the volume was completed to 15 mL with distilled water. 2 mL of oleic acid and 30 mL of toluene were added to the solution, obtaining a biphasic system with some suspended metal hydroxides (Zn (OH)$_2$ and Ga(OH)$_3$) in the aqueous phase. The mixture was transferred to a Teflon-lined stainless-steel autoclave and then heated at 160 °C for 24 h. The freshly synthesized zinc gallate nanoparticles (nZGO:Mn^{2+}) were precipitated with ethanol. Then, it was washed with ethanol and centrifuged four times (9000 rpm, 5 min). The precipitate had a brown color due to the presence of organic compounds coating the inorganic particles. The material was then annealed at 1150 °C (heating rate: 40 °C/min) for 30 min in a PYRO-Milestone Microwave system. Finally, white crystalline nZGO:Mn^{2+} particles were obtained after cooling, and further characterized with morphological, structural, and spectroscopic methods.

2.3. HPMC/nZGO:Mn^{2+} fabrication

The fabrication of HPMC/nZGO:Mn^{2+} films followed the process previously described [12]. Succinctly, 1 mg, 10 mg and 100 mg of the nanoparticles were mixed with 5 mL of HPMC aqueous solution (10 g/L) and dropped on a 10 cm^2 circle-shaped silicone rubber substrate mold, resulting in films containing 1 g/m^2, 10 g/m^2 and 100 g/m^2 of the persistent luminescence material. The mixture was left to dry over 24 h at 50 °C and the film was obtained (Fig. 1).

2.4. Characterization techniques

The X-ray diffraction (XRD) patterns of the samples were examined on Rigaku-Miniflex II XRD. The XRD measurements were performed at
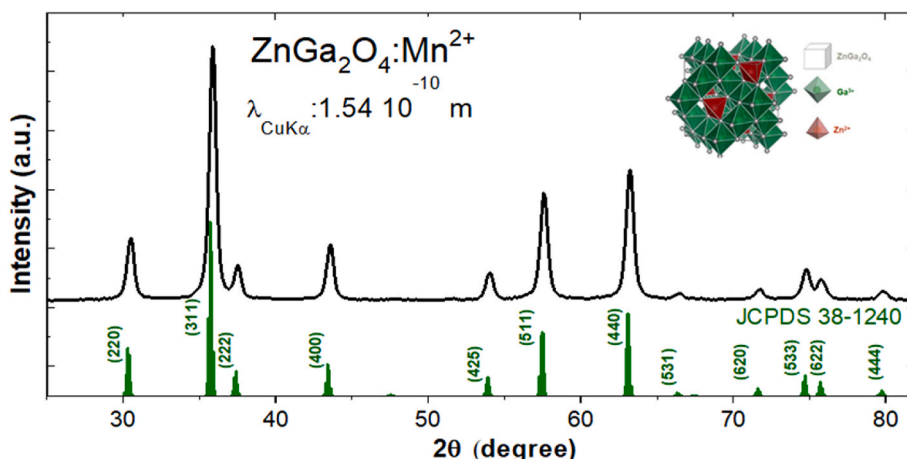

Fig. 2. XRD pattern of the nZGO:Mn^{2+} particles (black patterns) and standard pattern (JCPDS 38–1240).
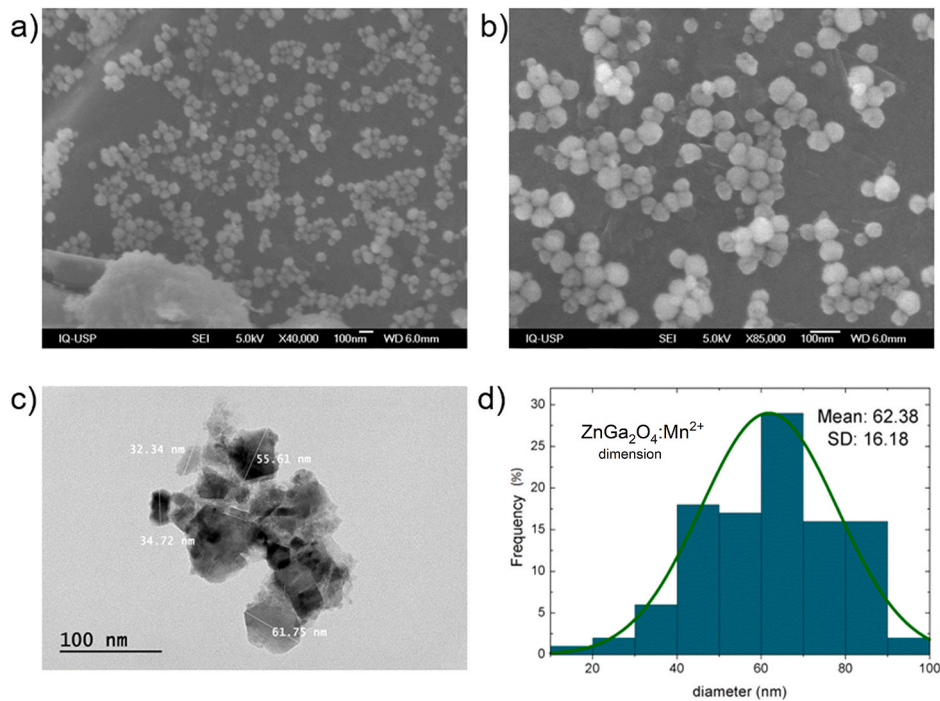
Fig. 3. (a) and (b) SEM images showing good size distribution of ZGONPs in aggregates. c) TEM image of ZGO particle with nanometric dimensions. (d) Particle size frequency graph obtained from analysis of 107 nanoparticles in SEM image.

room temperature using a copper anode as radiation source (CuKα = 1,54 Å, 30 kV and 40 mA), using a slit of 1 mm and CCD detector, step of 0.05 ° and scan speed of 0.05 °/s. Morphology of the samples was characterized by Scanning Electron Microscopy (SEM), using a JEOL JSM-740 1F microscope, and Transmission Electron Microscopy (TEM) using a MET JEOL JEM 2011. Isopropyl alcohol was used as a dispersing medium for SEM and TEM samples preparation followed by a 30 min sonication, then dropped on a carbon stub and copper grid, respectively, and dried before imaging. Excitation and emission spectra measurements and the afterglow decay curve measurement at room temperature

(300 K) were recorded in an Edinburgh Spectrometer FLS 1000 spectrophotometer equipped with a continuous 450 W Xenon lamp as excitation source. The measurements were simply carried out by 500 mg of the powder prepared as a thin-pressed pellet on a sample-holder. Electron Paramagnetic Resonance (EPR) measurements were carried out utilizing continuous wave Bruker EMX equipment at X-Band (9.5 GHz), 2 mW power and 7 G of modulation amplitude with a standard cavity at room temperature (295 K). The solid samples were accommodated at a 3 mm diameter quartz tube at room temperature (RT). EPR simulation of the sample was provided by the Easyspin [22] program and the
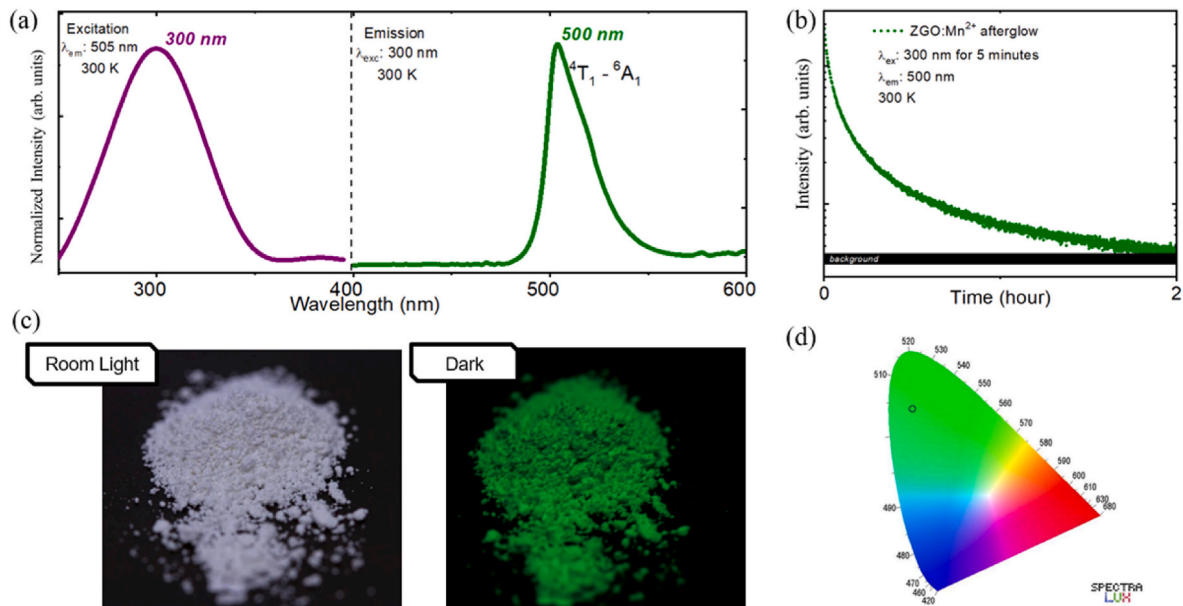

Fig. 4. (a) (left) Excitation spectrum of ZGO, emission monitored at 505 nm at 300 K; (right) Emission spectrum of ZGO, excitation monitored at 300 nm at 300 K. (b) Persistent Luminescence decay time of ZGO particles after 5 min charging at 300 nm, monitored at 500 nm. (c) Pictures of nZGO:Mn^{2+} under room light (left) and dark (right). (d) CIE Diagram of nZGO:Mn^{2+} emission created with SpectraLux [30].
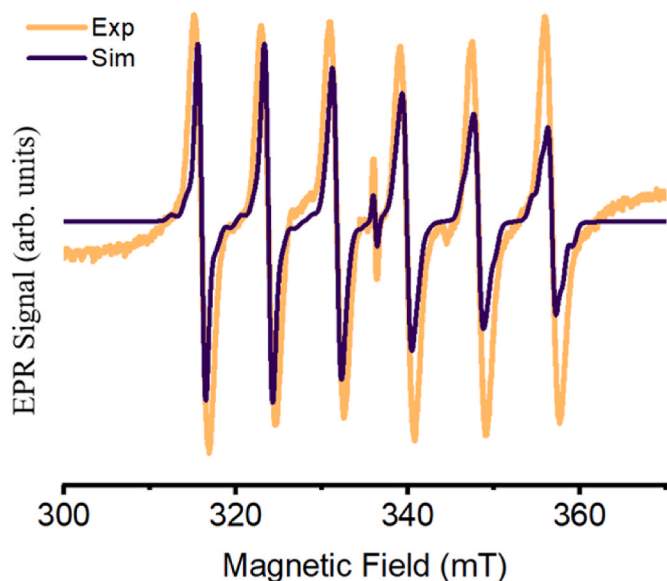
Fig. 5. EPR spectrum of $ZnGa_2O_4:Mn^{2+}$, experimental (orange) and simulated with Easyspin (purple). (For interpretation of the references to color in this figure legend, the reader is referred to the Web version of this article.)

SimultiSpin [23] program attached to Matlab software. The X-ray fluorescence (XRF) mapping and X-ray Excited Optical Luminescence (XEOL) mapping were carried out at Tarumã endstation of the Carnauba beamline from the Sirius Synchrotron facility (LNLS-CNPEM, Campinas-SP, Brazil) [24]. For these measurements, the films supported on aluminum frames were raster scanned at room temperature and ambient pressure with excitation energy of 12 keV. The XRF measurement used a Vortex SDD, 4 elements, Hitachi and the XEOL used an Ocean Optics QE Pro (200–950 nm) spectrometer. The XRF and XEOL data were treated using PyMCA as reported by Solé et al. [25].

3. Results and discussion

3.1. nZGO:Mn²⁺ nanoparticles

The nZGO:Mn²⁺ diffractogram is in accordance with the crystallographic data for $ZnGa_2O_4$ indexed at the Joint Committee on Powder Diffraction Standards (JCPDS), card #38–1240 (Fig. 2). No phase segregation from the presence of the Mn²⁺ was observed. As shown in the SEM (Fig. 3a and b) and TEM (Fig. 3c) images, the produced nanoparticles have a cubic-shaped morphology with high homogeneous distribution with average size 62 ± 16 nm (Fig. 3d). Even though aggregates of nanoparticles are formed - which is expected due to high temperature annealing procedure - the aggregates did not grow bigger than 300 nm. The TEM micrograph reveals, with high resolution, the
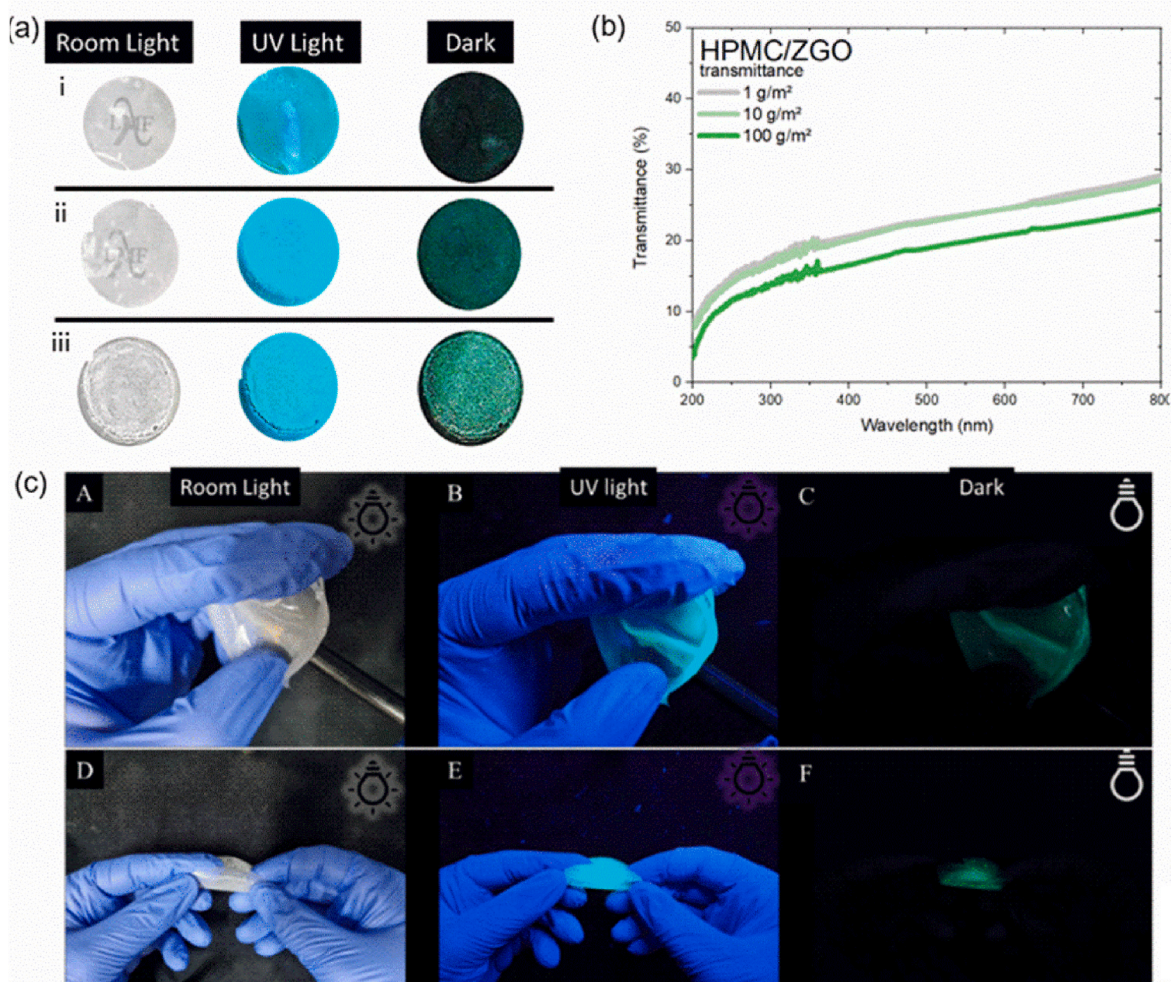

Fig. 6. (a) HPMC films with 1 mg of *nZGO:Mn²⁺* under room light, UV light, and Dark; (b) transmittance spectra of HPMC/nZGO materials. (c) HPMC films with 10 mg of *nZGO:Mn²⁺* under room light (A), UV light (B) and Dark (C) and HPMC films with 100 mg of *nZGO:Mn²⁺* under room light (D), UV light (E), and Dark (3).
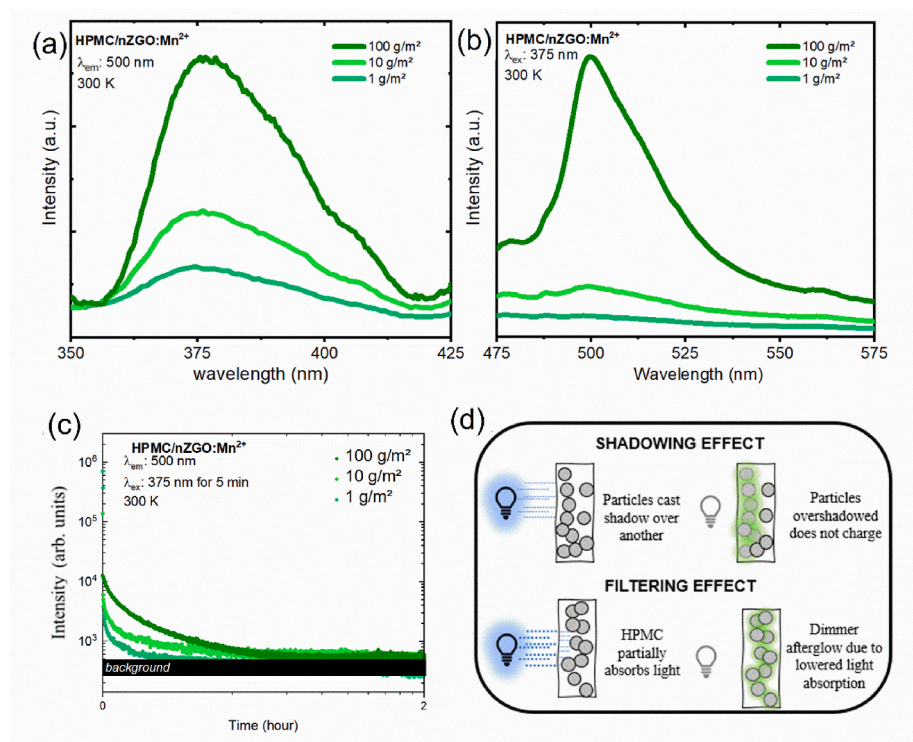
Fig. 7. (a) Excitation spectrum of HPMC/nZGO:Mn^{2+} thin composite film with different nanoparticle concentrations. (b) Emission spectrum of HPMC/nZGO:Mn^{2+} thin composite film with different nanoparticle concentrations. (c) Persistent luminescence spectrum of HPMC/nZGO:Mn^{2+} thin composite film. (d) Visual explanation of shadowing effect and filtering effect.

shape of a single crystallite and the nanometric size of the produced particles. Both particle shape and particle size observed in this TEM micrograph coincide with those shown previously in SEM micrographs.

The photoluminescence spectra of nZGO:Mn^{2+} measured with high spectral resolution at room temperature are shown in Fig. 4a. The excitation spectrum (λ_{em} = 505 nm) shows an excitation band in the ultraviolet (UV) spectral range with a maximum at 300 nm, which could be related to absorption around the band-gap energy in the spinel ZGO host (~4.4 eV) [26]. The strong green emission band is assigned to the spin-forbidden $^4T_1 \rightarrow {}^6A_1$ transition, which is the first excited energy state and the fundamental energy state of the Mn^{2+}, respectively, as shown on Tanabe-Sugano diagram for d^5 metals in high-spin state [27, 28]. After irradiating the nZGO:Mn^{2+} powders for 5 min at UV wavelength (300 nm) it shows persistence luminescence during more than 2 h at green region (500 nm) up to the limit of the equipment detection (Fig. 4b–d). This long time indicates that these nanoparticles are efficient in trapping charge carriers after UV excitation. Although the exact defect nature for these Mn^{2+}-doped materials are not well known, for Cr^{3+}-doped materials, the main traps are spinel anti-site defects as reported by Bessière et al. [29].

Regarding the lattice structure, it is expected that Mn^{2+} preferentially occupies Zn^{2+} sites in ZGO spinel [17]. This preferential substitution occurs not only due to charge similarity but also due to ionic radii match. Mn^{2+} radius in tetrahedral sites (CN = 4) is 0.66 Å and in octahedral sites (CN = 6) is 0.83 Å, while Zn^{2+} (CN = 4) and Ga^{3+} (CN = 6) radii are 0.6 Å and 0.62 Å, respectively.

EPR measurements of solid ZGO:Mn^{2+} were registered showing the expected six line EPR signal characteristic for the Mn^{2+} species, with a nuclear spin of 5/2 (Fig. 5). The spectra showed a clear isotropic Mn^{2+} signal, with six split bands corresponding to g constant equal to 2.0132 and A equal to 82 G. A signal corresponding to an unpaired electron on g equal to 2.0160 is also observed. It is possible to notice shoulder peaks at the manganese signal, which could be interpreted in two different ways: (i) an indicative of a second Mn^{2+} species with a slightly different

chemical environment, in this case Ga^{3+} octahedral site, instead of the Zn^{2+} tetrahedral site, resulting in a partial inverse spinel [31,32]; (ii) a zero-field splitting due to magnetic interaction between two manganese centers, or even the interaction between unpaired electrons belonging to the same Mn^{2+} $3 d^5$ orbital. Although zero-field splitting due to two manganese centers is more commonly reported for Mn^{3+} high spin species [33–35], it is also known for Mn^{2+} [36].

Using the Easyspin platform to simulate the EPR data, it was possible to determine that the shoulder peaks shown on the EPR spectrum are from the magnetic interaction between unpaired electrons belonging to the same Mn^{2+} center. A single Mn^{2+} species was settled using the described parameters above, adding a zero-field tensor, D, equal to 5.76 10^{-4} cm^{-1}. The simulation configuration, as shown in Fig. 5, matches the experimental spectrum, leading us to believe that the Manganese occupies only the zinc site.

3.2. HPMC/nZGO:Mn^{2+} films

The film composites formed by HPMC and *nZGO:Mn^{2+}* exhibit the characteristic green emission and persistent luminescence observed in solid nanoparticles. The films demonstrate acceptable transparency under room light, with a green emission like the solid particles (Fig. 6a). To evaluate the films' transparency quantitatively, we measured their transmittance across a range of wavelengths from 200 nm to 800 nm (Fig. 6b). The mean transmittance in the visible range (400 nm–700 nm) for films containing 1 mg, 10 mg, and 100 mg of *nZGO:Mn^{2+}* was 24%, 23%, and 20%, respectively. Besides the increased amount of nanoparticles that scatter light, one other reason for the decrease in transmittance (from 1 to 100 g/m²) is the increase in the film thickness with concentration: 18, 24 and 30 μm for the 1, 10 and 100 g/m², respectively. The films also exhibit remarkable flexibility, as demonstrated by their ability to be bent by hand without breaking (Fig. 6c).

The excitation and emission spectra of the composites depicts patterns similar to the ones observed for pure luminescent particles (Fig. 7a
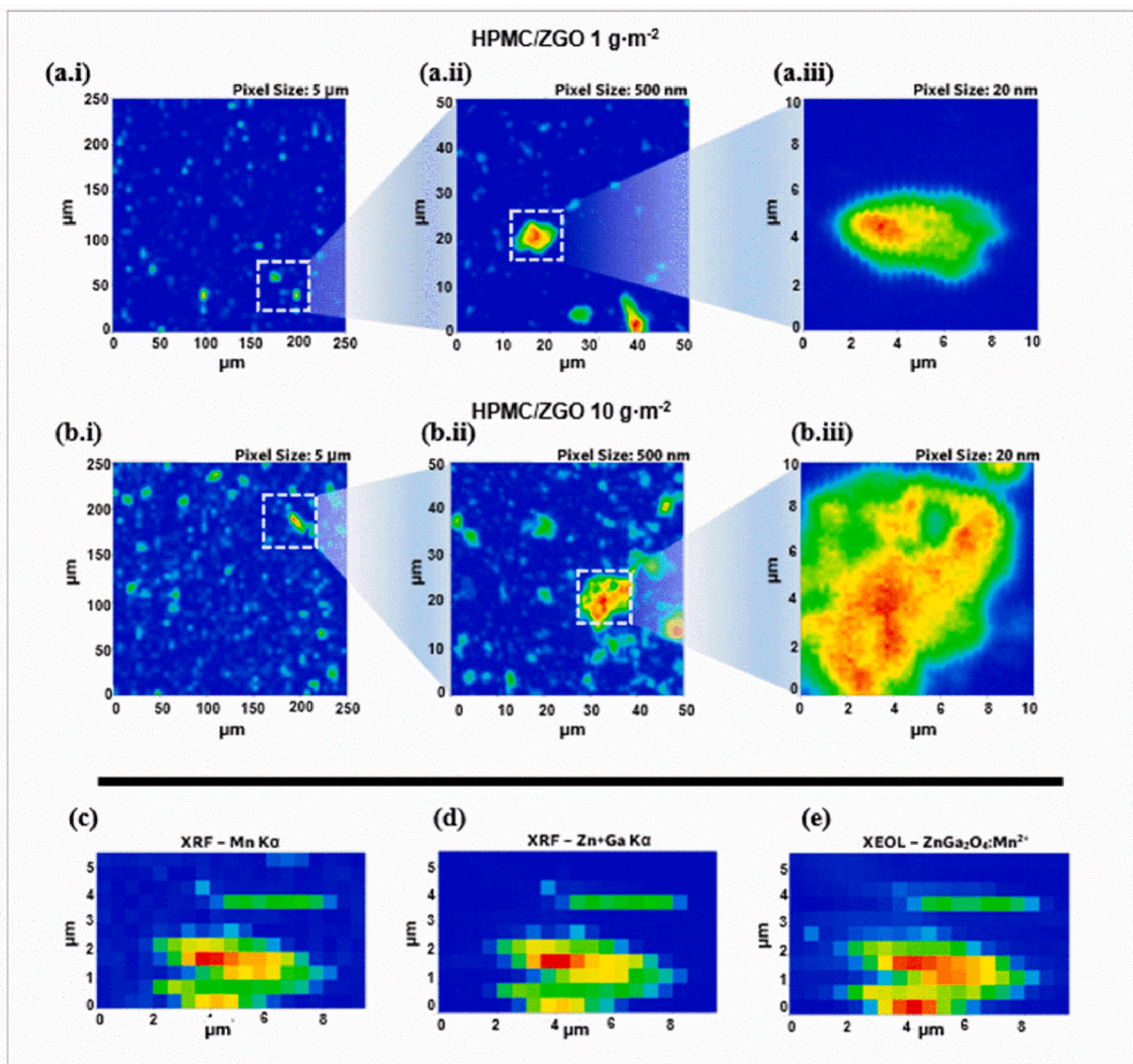
Fig. 8. a) XRF nanomaping images of HPMC/nZGO:Mn^{2+} in the surface concentration of 1 g/m^2 of the particles in three different magnifications (pixel size = 5 μm, 500 nm and 20 nm). b) XRF nanomaping images of HPMC/nZGO:Mn^{2+} in the surface concentration of 10 g/m^2 of the particles in three different magnifications. c) Mn Kα and d) Zn + Ga Kα XRF mapping of the 10 g/m^2 film registered simultaneously with the e) XEOL mapping.

and b). However, Mn^{2+} excitation spectrum is shifted, with its maximum now around 375 nm instead of 300 nm. This happens due to the absorption of HPMC, the major compound in the composite film, which starts around 350 nm and increases with smaller wavelengths [37], leading to the excitation shift as all incident photons are absorbed by HPMC and do not lead to Mn^{2+} emission, which is also known as filtering effect [38] (Fig. 7d). The green emission observed in the composites, as before, is attributed to the $^4T_1 \rightarrow {}^6A_1$ transition in nZGO: Mn^{2+}. The emission intensity as well as the afterglow duration decrease as the concentration of the particles in the film diminishes. The persistent luminescence duration (up to detector sensibility) ranges from 5 min for 1 g of particles per m^2 of film, to approx. 25 min for 10 g/m^2 reaching up to 2 h for the maximum concentration of 100 g/m^2, which is similar to the maximum persistent luminescent duration of the pure nZGO:Mn^{2+} powder (Fig. 7c). This indicates that no shadowing [39] effect takes place in these composites (Fig. 7d). This dampening effect take place due to the nanoparticles located closest to the surface of the film absorb more light than those located deeper in the film [39]. In our materials, probably due to the combination of small particle size and film thickness, we did not observe it.

Those findings reveal a significant relationship between the concentration of nanoparticles within the composite and the intensity of the emission/excitation bands. Specifically, as the concentration of nanoparticles decreases, the intensity of these bands also diminishes. This trend can be attributed to the reduced number of photons absorbed and emitted by the luminescent particles within the films, resulting in a weaker glow and a shorter afterglow duration. The decreased concentration of nanoparticles leads to a lower probability of photon capture, which ultimately limits the amount of emitted photons that can be detected.

To gain insight into the distribution of nanoparticles within the film, X-ray fluorescence (XRF) nano-mapping was registered on the films with nominal loading of 1, 10 and 100 g/m^2. The XRF mapping images (Fig. 8a and b) were generated integrating the Zn and Ga Kα fluorescence signals from the XRF spectra (Fig. S1) pixel by pixel. The results indicated that at both 1 and 10 g/m^2 nanoparticle loadings, the nanoparticles were evenly distributed throughout the film, except for a few clusters. Specifically, small, localized regions of higher nanoparticle concentration were observed, which may be attributed to the formation of water pockets during the HPMC film-casting process. These water pockets can lead to the formation of agglomerates. The agglomerates observed in this study had an approximate size of 6 μm, which is consistent with previous findings reported by our group. In a study of Sr$_2$MgSi$_2$O$_7$:Eu^{2+},Dy^{3+}/HPMC composites, we observed agglomerates

of the same size for the luminescent particles. This suggests that the formation of agglomerates may be a common phenomenon in the production of luminescent polymer composites, based on HPMC [12]. The 100 g/m^2 film exhibited very high particle concentration, covering almost the entire surface of the film composite (Fig. S2). The simultaneous XEOL and XRF nano-mapping measurement was also performed by integrating simultaneously the XEOL spectra (which exhibited only Mn^{2+} emission; Fig. S3) with the XRF at selected lines. The perfect superposition of XEOL and XRF signals suggest that Mn^{2+}-emission is only present at the same locations of Zn^{2+} and Ga^{3+}, which guarantees the integrity of the nanoparticles during the film casting (Fig. 8c–e).

4. Conclusions

In summary, ZnGa$_2$O$_4$:0,05mol%Mn^{2+} nanomaterials were successfully synthesized using a hydrothermal method followed by microwave annealing. XRD analysis confirmed the high purity and crystallinity of the spinel host, with no segregation or formation of undesired phases observed due to the incorporation of manganese. SEM and TEM images revealed uniform cubic nanocrystals of *n*ZGO:Mn^{2+}, with a mean size of 62.38 ± 16.18 nm. EPR analysis indicates that Mn^{2+} occupies only the tetrahedral site of the spinel. Moreover, the optical properties of the nanoparticles were found to be similar to those of the bulk material reported in the literature, as confirmed by excitation and emission analyses. The long-lasting persistence curve also demonstrated an afterglow duration of over 2 h at room temperature after UV-light irradiation ceased. These results suggest that *n*ZGO:Mn^{2+} nanoparticles have potential for use in optoelectronic applications, particularly as persistent luminescence materials. Nonetheless, the HPMC/*n*ZGO:Mn^{2+} composites presented applicable flexibility, and transparency with homogeneous distribution and no lixiviation of nanoparticles as shown by XRF and XEOL mappings. The PersL duration of the films increases with higher concentration of *n*ZGO:Mn^{2+} until the limit of pure nanoparticles. For the first time, HPMC/*n*ZGO:Mn^{2+} composites are reported featuring transparency and afterglow at the green region.

CRediT authorship contribution statement

Douglas L. Fritzen: Conceptualization, Methodology, Investigation, Writing – original draft, Writing – review & editing, Visualization. **Gabriel Nardy:** Methodology, Investigation. **Marcelo C. Portes:** Investigation, Formal analysis, Writing – review & editing. **Luidgi Giordano:** Writing – review & editing, Visualization. **Everton Bonturim:** Writing – review & editing, Supervision. **Verônica C. Teixeira:** Writing – review & editing, Investigation, Validation, Resources. **Lucas C.V. Rodrigues:** Conceptualization, Writing – review & editing, Supervision, Project administration, Funding acquisition.

Declaration of competing interest

The authors declare the following financial interests/personal relationships which may be considered as potential competing interests: Lucas Carvalho Veloso Rodrigues reports financial support was provided by State of Sao Paulo Research Foundation. Douglas Lourenco Fritzen reports financial support was provided by State of Sao Paulo Research Foundation. Veronica Carvalho Teixeira reports financial support was provided by State of Sao Paulo Research Foundation. Everton Bonturim reports financial support was provided by State of Sao Paulo Research Foundation. Lucas Carvalho Veloso Rodrigues reports financial support was provided by National Council for Scientific and Technological Development. Marcelo Cecconi Portes reports financial support was provided by National Council for Scientific and Technological Development. Veronica Carvalho Teixeira reports financial support was provided by National Council for Scientific and Technological Development. Luidgi Giordano reports financial support was provided by National Council for Scientific and Technological Development.

Data availability

Data will be made available on request.

Acknowledgements

Appendix A. Supplementary data

Supplementary data to this article can be found online at https://doi.org/10.1016/j.omx.2023.100271.

References

[1] Y. Katayama, H. Kobayashi, S. Tanabe, Deep-red persistent luminescence in Cr^{3+}-doped LaAlO$_3$ perovskite phosphor for in vivo imaging, APEX 8 (2015), 012102, https://doi.org/10.7567/APEX.8.012102/XML.

[2] D.O.A. dos Santos, L. Giordano, M.A.S.G. Barbará, M.C. Portes, C.C.S. Pedroso, V. C. Teixeira, M. Lastusaari, L.C.V. Rodrigues, Abnormal co-doping effect on the red persistent luminescence SrS:Eu^{2+},RE^{3+} materials, Dalton Trans. (2020), https://doi.org/10.1039/d0dt01315c.

[3] K. Van den Eeckhout, D. Poelman, P. Smet, Persistent luminescence in non-Eu^{2+}-doped compounds: a review, Materials 6 (2013) 2789–2818, https://doi.org/10.3390/ma6072789.

[4] K. Van den Eeckhout, P.F. Smet, D. Poelman, Persistent luminescence in Eu^{2+}-doped compounds: a review, Materials 3 (2010) 2536–2566, https://doi.org/10.3390/MA3042536.

[5] A.J.J. Bos, P. Dorenbos, A. Bessire, A. Lecointre, M. Bedu, M. Bettinelli, F. Piccinelli, Study of TL glow curves of YPO$_4$ double doped with lanthanide ions, Radiat. Meas. 46 (2011) 1410–1416, https://doi.org/10.1016/J.RADMEAS.2011.04.021.

[6] T. Maldiney, A. Lecointre, B. Viana, A. Bessière, M. Bessodes, D. Gourier, C. Richard, D. Scherman, Controlling electron trap depth to enhance optical properties of persistent luminescence nanoparticles for in vivo imaging, J. Am. Chem. Soc. 133 (2011) 11810–11815, https://doi.org/10.1021/JA204504W/SUPPL_FILE/JA204504W_SI_001.PDF.

[7] P. Dorenbos, Mechanism of persistent luminescence in Sr$_2$MgSi$_2$O$_7$:Eu^{2+}; Dy^{3+}, Phys. Status Solidi (2005) 242, https://doi.org/10.1002/PSSB.200409080. R7–R9.

[8] H.F. Brito, M. Malkamäki, L.C.V. Rodrigues, J. Hölsä, T. Laamanen, M. Lastusaari, Persistent luminescence mechanisms: human imagination at work, 2, Opt. Mater. Express 2 (4) (2012) 371–381, https://doi.org/10.1364/OME.2.000371, 371–381.

[9] J. Xu, S. Tanabe, Persistent luminescence instead of phosphorescence: history, mechanism, and perspective, J. Lumin. 205 (2019) 581–620, https://doi.org/10.1016/J.JLUMIN.2018.09.047.

[10] D. Van der Heggen, J.J. Joos, A. Feng, V. Fritz, T. Delgado, N. Gartmann, B. Walfort, D. Rytz, H. Hagemann, D. Poelman, B. Viana, P.F. Smet, Persistent luminescence in strontium aluminate: a roadmap to a brighter future, Adv. Funct. Mater. 32 (2022), 2208809, https://doi.org/10.1002/ADFM.202208809.

[11] D.L. Fritzen, L. Giordano, L.C.V. Rodrigues, J.H.S.K. Monteiro, Opportunities for persistent luminescent nanoparticles in luminescence imaging of biological systems and photodynamic therapy, Nanomaterials 10 (2020) 2015, https://doi.org/10.3390/NANO10102015, 10 (2020) 2015.

[12] D.L. Fritzen, E.A. de Mattos, D.F.S. Petri, V.C. Teixeira, E. Bonturim, L.C. V. Rodrigues, Flexible translucent persistent luminescent films based on $Sr_2MgSi_2O_7$:Eu^{2+},Dy^{3+} cellulose ether composites, Dalton Trans. 51 (2022) 9138–9143, https://doi.org/10.1039/D2DT00770C.

[13] X. Yang, B. Tang, X. Cao, The roles of dopant concentration and defect states in the optical properties of $Sr_2MgSi_2O_7$:Eu^{2+},Dy^{3+}, J. Alloys Compd. 949 (2023), 169841 https://doi.org/10.1016/J.JALLCOM.2023.169841.

[14] L.G. Merízio, E. Bonturim, R.U. Ichikawa, I.G.N. Silva, V.C. Teixeira, L.C. V. Rodrigues, H.F. Brito, Toward an energy-efficient synthesis method to improve persistent luminescence of $Sr_2MgSi_2O_7$:Eu^{2+},Dy^{3+}, Materialia (Oxf) 20 (2021), 101226, https://doi.org/10.1016/J.MTLA.2021.101226.

[15] V. Castaing, L. Giordano, C. Richard, D. Gourier, M. Allix, B. Viana, Photochromism and persistent luminescence in Ni-doped $ZnGa_2O_4$ transparent glass-ceramics: toward optical memory applications, J. Phys. Chem. C 125 (2021) 10110–10120, https://doi.org/10.1021/ACS.JPCC.1C01900/ASSET/IMAGES/LARGE/JP1C01900_0010.JPEG.

[16] T. Delgado, D. Rytz, G. Cai, M. Allix, E. Veron, I. di Carlo, B. Viana, Highly transparent Ce^{3+},Cr^{3+} co-doped GYAGG single crystals with enhanced persistent luminescence, Ceram. Int. (2023), https://doi.org/10.1016/j.ceramint.2023.02.249.

[17] A. Luchechko, Y. Zhydachevskyy, S. Ubizskii, O. Kravets, A.I. Popov, U. Rogulis, E. Elsts, E. Bulur, A. Suchocki, Afterglow, TL and OSL properties of Mn^{2+}-doped $ZnGa_2O_4$ phosphor, Sci. Rep. 9 (2019) 1–9, https://doi.org/10.1038/s41598-019-45869-7 (2019) 1–8.

[18] S.G. Menon, A.K. Kunti, D.E. Motaung, H.C. Swart, A new recipe for the rapid microwave synthesis of high quantum yield Mn^{2+}-doped $ZnGa_2O_4$ phosphors for potential forensic applications, New J. Chem. 43 (2019) 17446–17456, https://doi.org/10.1039/C9NJ04225C.

[19] Q. Zhou, L. Dolgov, A.M. Srivastava, L. Zhou, Z. Wang, J. Shi, M.D. Dramićanin, M. G. Brik, M. Wu, Mn^{2+} and Mn^{4+} red phosphors: synthesis, luminescence and applications in WLEDs. A review, J. Mater. Chem. C Mater. 6 (2018) 2652–2671, https://doi.org/10.1039/C8TC00251G.

[20] T. Si, Q. Zhu, J. Xiahou, X. Sun, J.G. Li, Regulating Mn^{2+}/Mn^{4+} activators in $ZnGa_2O_4$ via Mg^{2+}/Ge^{4+} doping to generate multimode luminescence for advanced anti-counterfeiting, ACS Appl. Electron. Mater. 3 (2021) 2005–2016, https://doi.org/10.1021/acsaelm.0c01121.

[21] B.B. Srivastava, A. Kuang, Y. Mao, Persistent luminescent sub-10 nm Cr doped $ZnGa_2O_4$ nanoparticles by a biphasic synthesis route, Chem. Commun. 51 (2015) 7372–7375, https://doi.org/10.1039/C5CC00377F.

[22] S. Stoll, A. Schweiger, EasySpin, a comprehensive software package for spectral simulation and analysis in EPR, J. Magn. Reson. 178 (2006) 42–55, https://doi.org/10.1016/j.jmr.2005.08.013.

[23] F. Molton, Simultispin: a versatile graphical user interface for the simulation of solid-state continuous wave EPR spectra, Magn. Reson. Chem. 58 (2020) 718–726, https://doi.org/10.1002/mrc.5019.

[24] H.C.N. Tolentino, R.R. Geraldes, F.M.C. da Silva, M.G.D. Guaita, C.M. Camarda, R. Szostak, I.T. Neckel, V.C. Teixeira, D. Hesterberg, C.A. Pérez, D. Galante, F. Callefo, A.C.P. Neto, L.M. Kofukuda, A.P.S. Sotero, G.B.Z.L. Moreno, S.A.L. Luiz, C.S.N.C. Bueno, F.R. Lena, H. Westfahl, The CARNAÚBA X-ray nanospectroscopy beamline at the Sirius-LNLS synchrotron light source: developments, commissioning, and first science at the TARUMÃ station, J. Electron. Spectrosc.

[25] Relat. Phenom. 266 (2023), 147340, https://doi.org/10.1016/J.ELSPEC.2023.147340.

[25] V.A. Solé, E. Papillon, M. Cotte, P. Walter, J. Susini, A multiplatform code for the analysis of energy-dispersive X-ray fluorescence spectra, Spectrochim. Acta Part B At. Spectrosc. 62 (2007) 63–68, https://doi.org/10.1016/J.SAB.2006.12.002.

[26] I.K. Jeong, H.L. Park, S. Il Mho, Photoluminescence of $ZnGa_2O_4$ mixed with $InGaZnO_4$, Solid State Commun. 108 (1998) 823–826, https://doi.org/10.1016/S0038-1098(98)00456-6.

[27] J.S. Kim, J.S. Kim, T.W. Kim, S.M. Kim, H.L. Park, Correlation between the crystalline environment and optical property of Mn^{2+} ions in $ZnGa_2O_4$: Mn^{2+} phosphor, Appl. Phys. Lett. 86 (2005) 1–3, https://doi.org/10.1063/1.1869550/328827.

[28] V.T. Gritsyna, Y.G. Kazarinov, V.A. Kobyakov, K.E. Sickafus, Defects and radiation induced electronic processes in magnesium aluminate spinel of different compositions, Radiat. Eff. Defect Solid 157 (2010) 659–663, https://doi.org/10.1080/10420150215784.

[29] A. Bessière, S.K. Sharma, N. Basavaraju, K.R. Priolkar, L. Binet, B. Viana, A.J.J. Bos, T. Maldiney, C. Richard, D. Scherman, D. Gourier, Storage of visible light for long-lasting phosphorescence in chromium-doped zinc gallate, Chem. Mater. 26 (2014) 1365–1373.

[30] F.S. Teles, P.A. Santa-Cruz, Spectra Lux Software v. 2.0, 2003.

[31] J. Popović, B. Gržeta, B. Rakvin, E. Tkalčec, S. Vrankić, S. Kurajica, Partial inverse spinel structure of manganese-doped gahnite: XRD and EPR spectroscopy studies, J. Alloys Compd. 509 (2011) 8487–8492, https://doi.org/10.1016/j.jallcom.2011.06.006.

[32] J.S. Shaffer, H.A. Farach, C.P. Poole, Electron-spin-resonance study of manganese-doped spinel, Phys. Rev. B 13 (1976) 1869–1875, https://doi.org/10.1103/PhysRevB.13.1869.

[33] B.J. Kennedy, K.S. Murray, Magnetic properties and zero-field splitting in high-spin manganese(III) complexes. 1. Mononuclear and polynuclear Schiff-base chelates, Inorg. Chem. 24 (1985) 1552–1557, https://doi.org/10.1021/ic00204a029.

[34] S. Mossin, H. Weihe, A.-L. Barra, Is the axial zero-field splitting parameter of tetragonally elongated high-spin manganese(III) complexes always negative? J. Am. Chem. Soc. 124 (2002) 8764–8765, https://doi.org/10.1021/ja012574p.

[35] D.V. Behere, S. Mitra, Magnetic susceptibility study and ground-state zero-field splitting in manganese(III) porphyrins, Inorg. Chem. 19 (1980) 992–995, https://doi.org/10.1021/ic50206a039.

[36] J. Reedijk, F.W. Klaaijsen, H.T. Witteveen, Zero-field splitting in tetragonal di-iodotetrakis(pyrazole)-manganese(II), J. Chem. Soc., Faraday Trans. 2 (69) (1973) 1537, https://doi.org/10.1039/f29736901537.

[37] S.B. Suma, Y. Sangappa, Fabrication and characterization of HPMC-AuNPs nanocomposite films, Mater. Today: Proc. 54 (2022) 660–663, https://doi.org/10.1016/j.matpr.2021.10.361.

[38] B. Kilic, S. Turkdogan, A. Astam, S.S. Baran, M. Asgin, H. Cebeci, D. Urk, Graphene-based copper oxide thin film nanostructures as high-efficiency photocathode for p-type dye-sensitized solar cells, J. Photon. Energy 7 (2017) 1, https://doi.org/10.1117/1.JPE.7.045502.

[39] S. Yavshits, Calculation of fission fragment yields at low and intermediate energy fission, in: AIP Conf Proc, AIP, 2005, pp. 373–376, https://doi.org/10.1063/1.2137272.